AGU PUBLICATIONS

JGR

Journal of Geophysical Research: Oceans

RESEARCH ARTICLE

10.1002/2016JC012200

Key Points:
- Seasonal to decadal AMOC variability at 26°N could be monitored by a tall mooring on the western and a shallow mooring on the eastern boundaries
- This sparse, two mooring, array will not reproduce trends in the AMOC on climate time scales as simulated in climate models
- Deep measurements, spanning the ocean basin, are essential to capture future AMOC decline

Correspondence to:
G. D. McCarthy,
gerard.mccarthy@noc.ac.uk

Citation:
McCarthy, G. D., M. B. Menary, J. V. Mecking, B. I. Moat, W. E. Johns, M. B. Andrews, D. Rayner, and D. A. Smeed (2017), The importance of deep, basinwide measurements in optimized Atlantic Meridional Overturning Circulation observing arrays, *J. Geophys. Res. Oceans*, *122*, 1808–1826, doi:10.1002/2016JC012200.

Received 29 JUL 2016
Accepted 12 DEC 2016
Accepted article online 23 DEC 2016
Published online 10 MAR 2017

The importance of deep, basinwide measurements in optimized Atlantic Meridional Overturning Circulation observing arrays

G. D. McCarthy[1], M. B. Menary[2], J. V. Mecking[3], B. I. Moat[1], W. E. Johns[4], M. B. Andrews[2], D. Rayner[1], and D. A. Smeed[1]

[1]National Oceanography Centre, European Way, Southampton, UK, [2]Met Office Hadley Centre, Met Office, Exeter, Devon, UK, [3]University of Southampton, Waterfront Campus, European Way, Southampton, UK, [4]Rosentiel School of Marine and Atmospheric Science, University of Miami, Miami, Florida, USA

Abstract The Atlantic Meridional Overturning Circulation (AMOC) is a key process in the global redistribution of heat. The AMOC is defined as the maximum of the overturning stream function, which typically occurs near 30°N in the North Atlantic. The RAPID mooring array has provided full-depth, basinwide, continuous estimates of this quantity since 2004. Motivated by both the need to deliver near real-time data and optimization of the array to reduce costs, we consider alternative configurations of the mooring array. Results suggest that the variability observed since 2004 could be reproduced by a single tall mooring on the western boundary and a mooring to 1500 m on the eastern boundary. We consider the potential future evolution of the AMOC in two generations of the Hadley Centre climate models and a suite of additional CMIP5 models. The modeling studies show that deep, basinwide measurements are essential to capture correctly the future decline of the AMOC. We conclude that, while a reduced array could be useful for estimates of the AMOC on subseasonal to decadal time scales as part of a near real-time data delivery system, extreme caution must be applied to avoid the potential misinterpretation or absence of a climate time scale AMOC decline that is a key motivation for the maintenance of these observations.

1. Introduction

The Atlantic Meridional Overturning Circulation (AMOC) is a key mechanism in the redistribution of heat and freshwater by the climate system. The ocean transports a maximum of nearly 1.3 PW (1 PW = 10^{15} W) of heat poleward in the North Atlantic [*Bryden and Imawaki*, 2001] of which 90% is carried by the AMOC [*Johns et al*., 2011]. At 26°N, the Atlantic moves 1.2 Sv (1 Sv = 10^6 m^3 s^{-1}) of freshwater southwards—again over 90% is carried by the AMOC [*McDonagh et al*., 2015]. Changes in the AMOC have a profound influence on global and regional climate. Abrupt shutdowns and recoveries of the AMOC in the paleoclimate record have been associated with glacial and interglacial periods, respectively [*Dansgaard et al*., 1984]. Considering the CMIP5 (Coupled Model Intercomparison Project Phase 5) suite of coupled climate models, the Intergovernmental Panel for Climate Change (IPCC) regard a shutdown of the AMOC unlikely but, in response to anthropogenic emission of greenhouse gases, an AMOC decline in the 21st century is considered very likely [*Stocker et al*., 2013]. The observation of this AMOC decline, should it occur, would be another mark of evidence of how profoundly human activity is altering the climate system.

While the importance of the AMOC on climate time scales has been appreciated for some time, an emerging field is the importance of AMOC variability on shorter time scales. Aside from the likely long-term decline, knowledge of the strength and variability of the AMOC is important in understanding the evolution of future global and regional climate variations [e.g., *Drijfhout et al*., 2012; *McCarthy et al*., 2015a]. On even shorter time scales, the potential role of AMOC variability in seasonal climate prediction and accelerated sea level rise is an emerging possibility. Regarding the former, following large interannual variability in the AMOC the winter of 2009–2010 [*McCarthy et al*., 2012], the winter sea-surface temperature (SST) pattern that re-emerged in 2010–2011 [*Taws et al*., 2011] were sufficient to push the North Atlantic Oscillation (NAO) into a negative state [*Buchan et al*., 2014]. The correct initialization of these SST patterns was crucial to the successful seasonal forecast of that year's negative NAO [*Maidens et al*., 2013]. *Duchez et al*. [2015]

show that AMOC variations precede certain SST patterns and could thus feed into the predictions of these SSTs and improved seasonal forecasts, if near real-time AMOC estimates were available. Regarding the latter, following the dip in the AMOC in 2009/2010, sea level in New York rose by 10 cm 2 months later [*Goddard et al*., 2015]. This sea level increase was associated with a weakening of the geostrophic circulation of the North Atlantic, which keeps sea level low along the US east coast. This research points to the potential use of near real-time AMOC estimates in seasonal climate prediction and flooding risk assessment in certain locations.

The strength of the AMOC is typically defined as the maximum of the overturning stream function (Ψ):

$$\mathrm{AMOC} = \max(\Psi(z,y)) = \max\left(\int_0^z \int_{x_w}^{x_e} v(x,y,z')\,dx\,dz'\right), \quad (1)$$

where the meridional velocity (v) is integrated over longitude from west (x_w) to east (x_e) and depth (z) at each latitude (y). The basinwide, top-to-bottom integral of the meridional velocities, the throughflow, has been implicitly removed in this definition.

Since 2004, the AMOC has been continuously measured by the joint UK-US RAPID-MOCHA-WBTS array (hereafter referred to as the RAPID array) of 19 moorings consisting primarily of current meters and moored conductivity-temperature-depth (CTD) instruments [*Cunningham et al*., 2007]. The maximum of the overturning circulation typically occurs near 30°N in climate models [e.g., *Menary et al*., 2013] but 26.5°N was the preferred latitude for the RAPID array due to the long-running Florida Current measurements (since 1982) [*Meinen et al*., 2010] and a number of full-depth, basinwide hydrographic sections [*Bryden et al*., 2005] at this latitude. Continuous measurements of certain components of the AMOC have been made over a longer time period than the RAPID observations, such as the overflows across the Greenland-Scotland Ridge [*Hansen et al*., 2016] and outflow from the Labrador Sea [*Fischer et al*., 2010]. Other observing arrays, such as the MOVE array at 16°N [*Send et al*., 2011], the SAMBA array at 35°S [*Meinen et al*., 2013] and the OSNAP array north of 53°N [*Lozier et al*., 2016], provide estimates of the overturning circulation at different latitudes. But only the RAPID measurements provide the full-depth, basinwide observational estimate of the maximum of the overturning stream function as defined in equation (1).

The design of the RAPID array is based on combining directly estimated transports with transport estimated using the geostrophic thermal wind relationship [see *McCarthy et al*., 2015b, for a full description]. The directly estimated transports consist of the Florida Current estimates, direct current meter based observations in the 20 km over the Bahamas escarpment to approximately 76.75°W and Ekman transport derived from reanalysis winds. The thermal wind derived transports stretch from the eastern boundary to 76.75°W. The original array design experiments of, for example, *Hirschi et al*. [2003] and *Baehr et al*. [2004] showed that this geostrophic transport could be measured using a relatively sparse array of moorings. In fact, if the basin was vertically sided and flat-bottomed, just two moorings would be needed to capture the cross-basin density difference that defines the basinwide flow [*Hirschi and Marotzke*, 2007]. This geostrophic relationship forms the basis of hydrographic estimates of the overturning circulation [e.g., *Bryden et al*., 2005] and some paleoceanography reconstructions of the overturning [*Lynch-Stieglitz*, 2001]. The fundamental dynamic captured by this geostrophic element of the RAPID array is that isotherms (and consequently isopycnals, as density is temperature dominated at this location) deepen to the west above 1000 m, defining the southward gyre flow, and, below 1000 m, the isotherms deepen to the east indicating further southward flow, with northward flowing intermediate water in between (Figure 1). The majority of the western boundary current is confined to the Florida Straits. These estimates of the Florida Current have shown less variability since measurements began in 1982 [*Meinen et al*., 2010] than has been seen in the RAPID estimates of the AMOC since 2004. Therefore, the circulation variability captured by the geostrophic element of the RAPID array is defined by a partition between shallow southward flow in the gyre and deep southward flow in the overturning [*McCarthy et al*., 2012]. The geostrophic array design is based on relatively few mooring because, in the absence of intervening topography, the density on either boundary is sufficient to resolve the basinwide thermal wind and, therefore, the key balance between southward gyre flow and southward deep flow. Hence, the moorings are focused on the eastern and western boundaries and on either side of the mid-Atlantic ridge.

In spite of its relative sparseness, the deployment and maintenance of the RAPID mooring array takes considerable resources and opportunities to provide accurate estimates of the AMOC for less expense are of

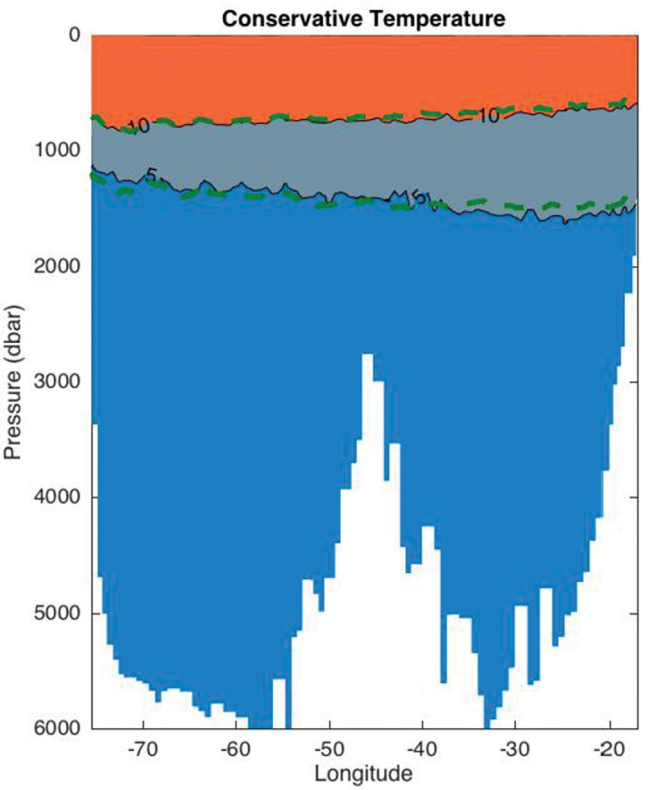

Figure 1. Simplified section of conservative temperature from 2004 at 24.5°N from east of the Bahamas escarpment to the eastern boundary highlighting the main overturning dynamics. Green, dashed lines overlaying the 5°C and 10°C show the 36.8 and 36 kg m^{-3} density contours.

interest [e.g., *Fischer et al.*, 2013; *Dunstone*, 2014]. One option is to use alternative measurements to moorings. This was the approach used by *Willis* [2010], who combined satellite and Argo measurements to estimate the overturning circulation near 40°N, a latitude that fulfils the prerequisite of this method that there is little transport over shallow topography. An estimate of the AMOC by *Frajka-Williams* [2015], combining satellite-based sea-surface height (SSH) estimates offshore of the Bahamas with Florida current data, extended estimates of the AMOC back to 1993. The primary signal that is captured in the SSH is the first baroclinic mode [*Szuts et al.*, 2012] and provides information about the ocean structure in the top 1000 m away from the boundaries. This has proved to correlate highly with the full-depth estimates from the RAPID array [*Frajka-Williams*, 2015].

In contrast to these essentially thermocline-based estimates of the AMOC, a number of studies have emphasized the utility of subsurface proxies for the strength of the AMOC [*Baehr et al.*, 2007; *Zhang*, 2008; *Roberts et al.*, 2013]. In particular, *Baehr et al.* [2007] highlighted cross-basin, deep density difference as a useful proxy for detecting long-term changes in the AMOC. This leads us to ask the question: Can a reduced mooring array capture both seasonal-to-decadal and climate time scale variability in the AMOC?

We will address this question from two angles. First, 10 years of data from the RAPID array [*Smeed et al.*, 2015] is subsampled to see how reduced data can be used to make estimates of the AMOC by comparing the accuracy of this reduced array to full array estimates. Second, we look at the problem on longer time scales by assessing a range of climate model runs that show future declines in the AMOC in response to anthropogenic climate change to ask whether the RAPID array style sampling (or sampling from a reduced array) is able to capture the simulated future changes in the AMOC.

2. The Design of a Minimal Array

The RAPID array estimates the basinwide integrated geostrophic transport across the basin. Large-scale ocean circulation is in geostrophic balance so the meridional transport across an ocean basin can be calculated from the difference in pressure between eastern and western boundaries and across any intervening ocean ridges. The stream function for the flow can be expressed as:

$$\Psi(z) = \frac{1}{\rho_0 f}\int_{z_R}^{z} dz' \Delta P(z'), \tag{2}$$

where

$$\Delta P(z) = P_E(z) - P_W(z)$$

is the cross-basin pressure difference, f is the Coriolis parameter and ρ_0 is a reference density. The RAPID calculation combines a number of moorings close to the western boundary, on either flank of the mid-Atlantic ridge and along the eastern boundary to construct temperature and salinity profiles representative of these

locations. These profiles are used to calculate density (ρ) and dynamic height (Φ), which is related to the pressure by

$$P(z)-P(z_R)=-g\int_{z_R}^{z} dz'\rho(z')=\rho_0\Phi(z), \tag{3}$$

where g is gravity and the level z_R is a reference level. In practice, dynamic height is used in the calculations but, for the development of the theory here, we are interested in the nonintegrated quantity to assess the impact of changes at arbitrary levels on the AMOC and so we focus on using density to detect the pressure gradient. The two main pressure gradients at 26.5°N is the east-west basinwide pressure difference and the pressure difference across the mid-Atlantic Ridge. The pressure gradient across the mid-Atlantic ridge is much smaller than that between the eastern and western boundaries. We will focus on the east-west balance to develop this theory before considering these other elements.

In addition to the estimates of geostrophic shear based on density, direct current meter measurements near the western boundary estimate the flow west of 76.75°W. This region is referred to as the Western Boundary Wedge (WBW).

The estimate of the circulation used in the RAPID calculation uses zero net flow across the section to constrain the velocity field [*Kanzow et al*., 2007]. This constraint has been independently verified, within an accuracy of approximately 1 Sv, in models [*Hirschi and Marotzke*, 2007], by bottom pressure recorder data [*Kanzow et al*., 2007] and gravity satellite, GRACE, data [*Landerer et al*., 2015].

We show in Appendix A, the impact of small changes in the cross-basin density difference at a given depth on the overturning stream function can be expressed as:

$$\Delta\Psi=\frac{g}{\rho_0 f}\int_{z_R}^{0} dz' G_\Psi(z,z')\Delta\rho(z'), \tag{4}$$

where G_Ψ is a Green's function, given by

$$G_\Psi(z,z')=\begin{cases} z-z'+\dfrac{A(z)}{A}z' & z>z' \\ \dfrac{A(z)}{A}z' & z<z' \end{cases}, \tag{5}$$

where

$$A(z)=\int_{z_R}^{z} w(z')dz'$$

is the area derived from integrating the basin width, $w(z)$, from the seafloor to depth z. $A(0)=A$ is the full area across the basin. The fraction $A(z)/A$ is the fraction of the basin cross-section deeper than z, which has a value of 1 at the sea-surface and zero at the seafloor. The impact on the AMOC is then approximated by the change at the depth of the maximum overturning:

$$\Delta\mathrm{AMOC}=\Delta\Psi|_{z=z_M}+O(\Delta\Psi^2).$$

The advantage of using this Green's function approach is to allow a direct assessment of a density change on the final value of the AMOC. As the density is twice integrated to derive a stream function, Figure 2 is a useful way of assessing the impact of density anomalies at given depths on the AMOC. The density anomalies are considered to have a 100 dbar extent. Changes on the east and west boundaries have equal and opposite impact, hence the symmetry around the zero density anomaly line. If the same change is made on the east as on the west, the AMOC is unchanged. So, for example, if the whole water column on both sides of the basin warms by the same amount, there would be no change in the AMOC. Density changes at the surface and seafloor have no effect on the AMOC. The maximum of $G_\Psi(z_M,0)$ is when $z=z_M$, indicating that density anomalies around the level of the AMOC maximum have the most impact. In the RAPID observations, this occurs near 1100 m [*McCarthy et al*., 2015b].

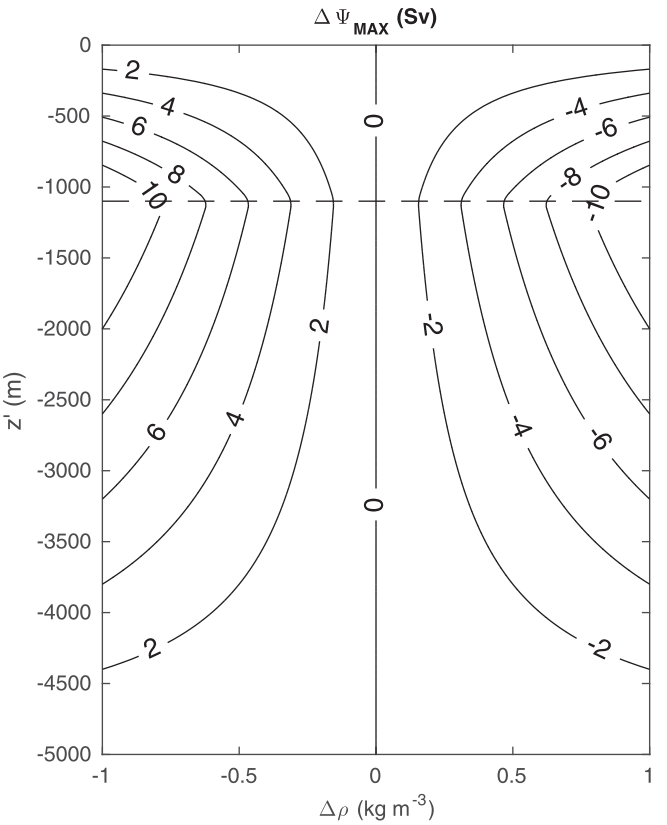

Figure 2. Changes in the maximum of the overturning stream fuction due to density anomalies at a given depth. Density anomalies are applied over a 100 dbar range.

We can use the Green's function to estimate the amount of variance in the AMOC due to the variability of density at each level on the eastern and western boundaries. If

$$f(z)=\mathrm{var}(\rho(z))[G_\Psi(z_M,z)]^2,$$

then

$$F(z_1,z_2)=\frac{\int_{z_1}^{z_2} dz' f(z')}{\int_{z_R}^{0} dz' f(z')} \quad (6)$$

is the fraction of variance in the AMOC due to density variations between z_1 and z_2. Note that this analysis does not take account of the covariances between density variations at different locations and so provides only an approximation to the total AMOC variance.

So far, we have only considered the situation of transport between the eastern and western boundaries. At 26.5°N, there are the added components of the pressure gradient across mid-Atlantic ridge and the transport in the WBW. To assess the impacts of these components of the RAPID calculation, the following approach is taken. Dynamic height profiles are constructed, as described in *McCarthy et al*. [2015b] for the eastern and western boundaries and for the eastern and western flanks of the mid-Atlantic ridge. The vertical derivative of this is calculated to relate back to the density (equation (3)). The density gradient between the eastern and western boundaries is considered as is the gradient between the eastern and western flanks of the mid-Atlantic ridge. The contributions from the eastern and western boundaries individually are considered, relative to the mean. For the WBW, a proxy for dynamic height is constructed by multiplying the transport profile, $T(z)$, by the Coriolis parameter to give an equivalent of dynamic height difference across the WBW:

$$T(z)=\frac{\Phi^*(z)}{f}.$$

This element can then be treated similarly to the other elements of the calculation.

Figure 3 shows the fraction of AMOC variance as estimated using equation (6). The variance from the eastern and western boundaries, the mid-Atlantic ridge and the WBW are shown. Results indicate that a combination of the data from the top 1000 m of each component would describe 70% of the variance; data to 1500 m would describe over 90% of the variance, with the addition of data on the western boundary to 3500 m over 99% of the variability observed since 2004 is captured.

Data from the mid-Atlantic ridge contributes very little to the variability of the AMOC that has been observed. Given that over 70% of the variance observed is captured by the top 1000 m variability, the lack of variability from the mid-Atlantic ridge is hardly surprising. At levels shallower than the effective depth of the mid-Atlantic ridge, the mid-Atlantic moorings do not contribute to the basinwide transport [*McCarthy et al*., 2015b]. The effective height of the mid-Atlantic ridge is the depth at which pressure gradients cannot be transmitted from the eastern flank of the ridge to the western flank. The shallowest depth of the ridge occurs around 3000 m but deep pressure gradients are transmitted across the ridge to depths of around

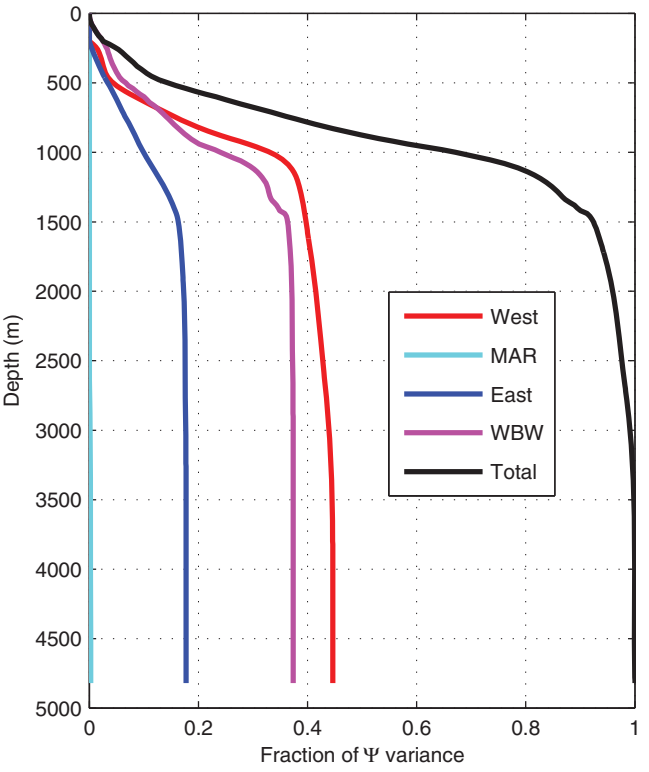

Figure 3. Fraction of variance of the AMOC estimate contributed the mid-Atlantic ridge (cyan), eastern boundary (blue), WBW (magenta), western boundary (red), and the sum of these components (black).

3700 m [*Cunningham et al.*, 2007]. The deep measurements on either side of the ridge aim to capture variations in Antarctic Bottom Water [*Frajka-Williams et al.*, 2011], which have not varied significantly over the observational period [*McCarthy et al.*, 2015b].

3. Assessment of Minimal Array Design

The analytical insight from the Green's function analysis can be translated into a design for a sparse array by examining the moorings in Figure 4. The eastern and western dynamic height measurements are easily addressed. On the western boundary, the mooring WB2 provides surface to 3800 m coverage of the density profile. On the eastern boundary, the moorings EBH4 (EBH3) covers the top 1000 m (1500 m).

The Western Boundary Wedge is composed of current meter measurements from four moorings (WBADCP, WB0, WB1, and WB2, see Figure 4) to estimate the transport from the continental shelf to WB2 [*Johns et al.*, 2008]. To estimate the transport using as few moorings as possible, we investigate the correlations between the overall transport in the WBW and the individual moorings. There is a high degree of correlation between the velocity profiles at each of the moorings west of and including WB2 and the total WBW transport. This is not altogether surprising as the WBW is not independent of the individual moorings and eddy noise decreases toward to boundary [*Kanzow et al.*, 2009], hence higher correlation might be expected.

To estimate a WBW transport from current meters on the WB2 and other moorings, we calculate the amplitude of the first principal components of the full transport in the wedge, calculate the amplitudes of the first four principal components of the velocity profile at WB2 and other moorings. We then use multiple regression to model the first PC of the transport as a function of the four principal components of the WB2 velocity profile. The results are shown in Figure 5. The residual error has a standard deviation of 0.55 Sv relative to the standard deviation of the full transport of 2.51 Sv.

We consider a number of sparse array designs to quantitatively estimate their ability to reproduction of the AMOC variability. The four configurations considered are described in Table 1. These calculate the AMOC when variations in density on either side of the basin are restricted to a given depth range or when the WBW moorings are fully included or a reconstructed version is considered.

Figure 6 shows the difference between each version of the reduced array and the full RAPID calculation of the AMOC. The results support those of the Green's function analysis. Using only data from the upper 1000 (1500) m, RS1000 (RS1500), respectively, results in a residual variance of 0.84 Sv^2 (0.63 Sv^2) relative the full calculation. This shows that most of the variance of the AMOC that has been observed since 2004 is contained in the upper ocean. The best reproduction of the full calculation from a reduced array is the RSW configuration with a residual variance of 0.06 Sv^2. Finally, the RSW-mod configuration results in a transport estimate with a residual variance of 0.17 Sv^2.

This final combination has a slightly higher error variance than using the full wedge but offers the appeal that the AMOC can be estimated using a single tall mooring on the western boundary at WB2 (to a depth of

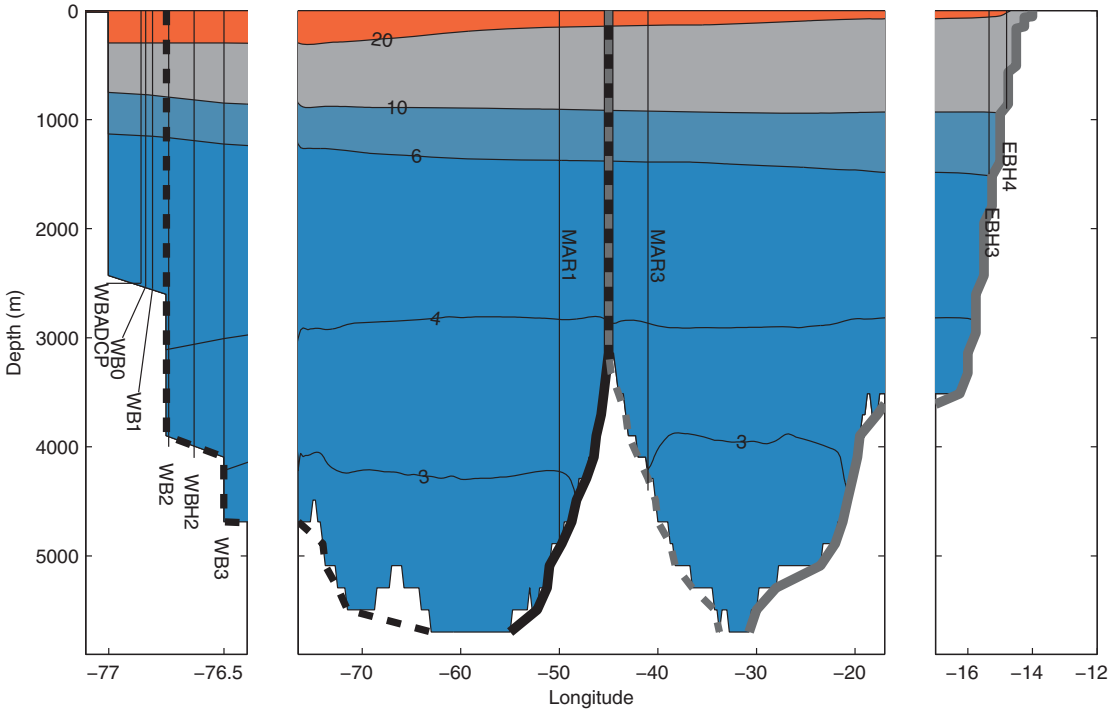

Figure 4. Mean potential temperature section at 26.5°N in the HG3 model prior to 2005. Vertical black lines indicate the location of selected moorings in the RAPID array. The locations of model output used to construct profiles for the western and eastern boundaries and western and eastern flanks of the mid-Atlantic ridge are indicated with black-dashed; gray-solid; black-solid; and gray-dashed lines, respectively. Approximate locations of moorings that comprise the WBW (WBADCP, WB0, WB1, WB2), the western boundary (WB2, WBH2, WB3), western (MAR1), and eastern (MAR3) flanks of the Mid-Atlantic Ridge and the eastern boundary (EBH3, EBH4) are indicated. These are proximate locations only.

3800 m) and a single mooring on the eastern boundary at EBH3 (to a depth of 1500 m) in combination with the cable estimates from the Florida Current and reanalysis based Ekman transport estimates.

4. Minimal Arrays and the Measurement of Future Changes

The previous section has shown that it is possible to reconstruct the vast majority of observed AMOC variability since 2004 as estimated by the full RAPID array using a much reduced array of moorings. However, on climate time scales, a decade is a short period of time. To address the question of the ability of minimal arrays to measure long-term changes in the AMOC, we simulate a RAPID-analog calculation in a range of climate models that show future AMOC declines. We then consider certain minimal array configurations to assess whether long-term changes are captured.

The AMOC is expected to decline due to anthropogenic forcing in the coming century [*Stocker et al*., 2013]. However, there is a range of rates of decline seen in a range of CMIP5 models. While it is not possible to know whether the mechanism of AMOC decline in any one of these models will represent the behavior of a future decline in the AMOC, these models are still the best tool for investigating future changes in the climate system and in the AMOC. Any minimal array design would need to be able to capture future declines in the overturning circulation or the main goal of the observing array would be lost.

We consider a number of CMIP5 models that show future declines in the AMOC under two different emissions scenarios RCP 4.5 and RCP 8.5, where RCP is Representative Concentration Pathway (e.g., RCP 8.5 is intended to result in a net top of atmosphere radiative imbalance of 8.5 W m^{-2} in the year 2100). The models analyzed are ACCESS 1.0, ACCESS 1.3, CSIRO-Mk3, CanESM2, MPI-LR, MPI-MR and two generations of the HadGEM model: HadGEM2-ES and HadGEM3-GC2 (Table 2). We analyze the two HadGEM models in further detail. These two models were chosen for this study as they both show a distinct future declines in the AMOC and comprise two generations of climate models and thus provide a wide sample of the parameter space.

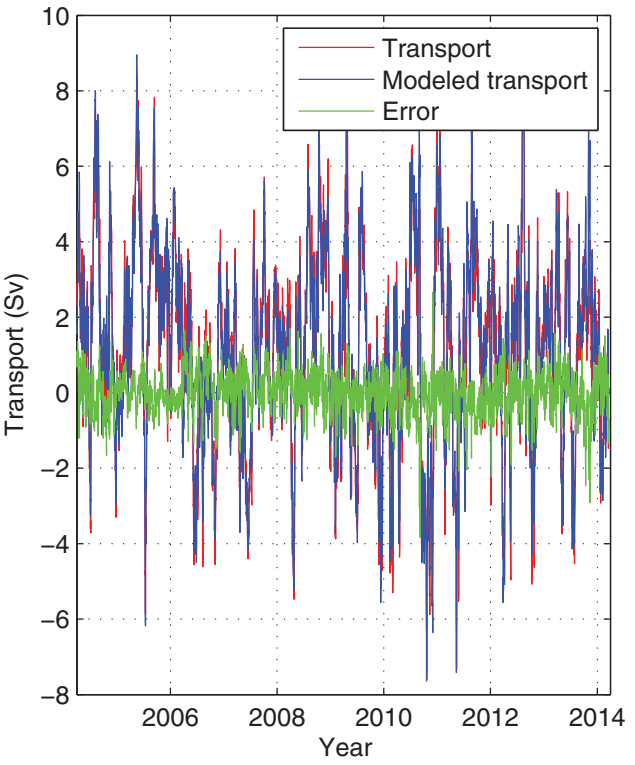

Figure 5. The full transport in the WBW (red) as modeled on the EOF relationship between the full transport and the WB2 mooring (blue). The difference (green) has a standard deviation of 0.55 Sv.

The version of HadGEM2-ES used in this analysis has an ocean resolution of 1° rising to 1/3° in latitude near the equator and has 40 *z*-coordinate vertical levels [*Collins et al.*, 2011]. The ocean model is based on an updated version of the ocean module used in the HadCM3 model. The model is forced with historical estimates of greenhouse gas concentrations, solar variability, land use changes, and volcanic and anthropogenic aerosols until 2005. Between 2005 and 2100 the model is forced with projected future changes in the same consistent with the RCP 8.5 forcing scenario [see *Jones et al.*, 2011, for further details]. The atmospheric component has a resolution of 1.25° × 1.875° with 38 vertical levels. We refer to this model as HG2 from here onwards.

The state-of-the-art coupled climate model HadGEM3-GC2 [*Williams et al.*, 2015] is the same model configuration used in the operational seasonal and decadal forecast systems of the Met Office (GloSea5 and DEPRESYS3). The ocean model is the Global Ocean 5.0 [*Megann et al.*, 2013] version of the v3.4 NEMO model [*Madec*, 2008] and uses the ORCA025 tripolar grid configuration. It has 75 vertical levels, and a nominal horizontal resolution of 0.25 degrees. The RCP 4.5 scenario differs in configuration from the present day control simulation [*Jackson et al.*, 2015] as it uses CMIP5 RCP4.5 forcing data sets [*Jones et al.*, 2011]. This includes well-mixed greenhouse gases (CO_2, CH_4, N_2O, chlorofluorocarbons, and hydrofluorocarbons), tropospheric aerosols (including sulfates, soot, biomass aerosols, and organic carbon from fossil fuels), monthly varying tropospheric and stratospheric ozone concentrations, varying solar irradiance, and stratospheric volcanic aerosol at background levels [*Sato et al.*, 1993]. This simulation is a continuation of a historical simulation which uses CMIP5 historical forcings. The historical simulation ran from 1850 using initial conditions from a GC2 preindustrial control run. We refer to this model as HG3 from here on.

Figure 4 shows a mean potential temperature section from the HG3 model at the latitude nearest to 26.5°N in the North Atlantic. As described earlier, the RAPID calculation relies on calculating the boundary dynamic height along the western, eastern and on both sides of the mid-Atlantic Ridge to estimate geostrophic transport. The exception to this is wind-driven Ekman transport near the surface and direct current and velocity measurements from the WBW and the Florida Straits. In the HG3 analysis, the WBW limit is defined at 76.75°W at the same longitude as in the observational calculation [*McCarthy et al.*, 2015b]. West of this, including in the Florida Straits, direct velocity is used to calculate transport. At the WBW limit of 76.75°W and continuing down along the western boundary to the deepest part of the basin west of the mid-Atlantic ridge, a temperature and salinity profile is calculated (black, dashed line in Figure 4). This is an analog of the western boundary profile

Table 1. Configurations of Sparse Array Considered[a]

Short Name	East Depth	West Depth	WBW
RS1000	1000 m	1000 m	Full
RS1500	1500 m	1500 m	Full
RSW	1500 m	3800 m	Full
RSW-mod	1500 m	3800 m	Reconstructed

[a]East/west depth refers to the depth to which density variations are considered. Constant values are used below this depth. The WBW is either full or reconstructed as described in the text. "RS" refers to RAPID-style.

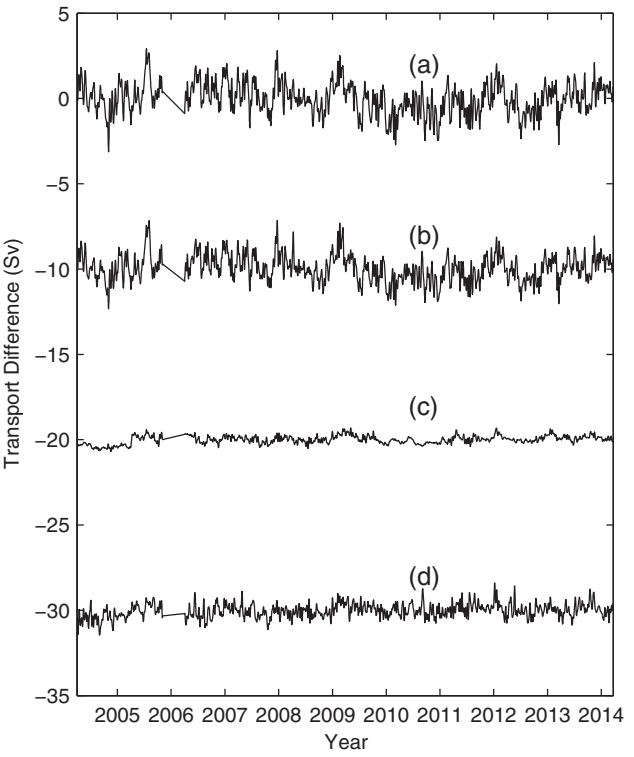

Figure 6. Reduced array AMOC strength minus full array AMOC strength, subsequent values offset by 10 Sv. Cases considered are (a) RS1000, (b) RS1500, (c) RSW, and (d) RSW-mod.

used in the observational calculation. Similarly, profiles for the western and eastern flanks of the mid-Atlantic Ridge and along the eastern boundary are constructed (Figure 4). Dynamic height from each of these "profiles" is calculated relative to a reference level. The reference level in the observational calculation is chosen to be at approximately the interface between northward and southward flowing water masses. We apply the same criteria in the model but use the basinwide integrated velocities to identify a suitable level between northward and southward flowing water masses. In the case of HG3 model, this reference level was chosen at 4600 m, where the basinwide transport profile, calculated from the full velocities, is zero. Geostrophic shear is calculated taking the difference in dynamic height between each of these profiles analogous to the description in *McCarthy et al.* [2015b]. Meridional Ekman transport is calculated from the zonal wind stress. The direct velocity west of 76.75°W, geostrophic shear and Ekman transports are combined with a compensation velocity term to ensure zero net transport across the section. The resulting transport profile is vertically integrated to give an overturning stream function, the maximum of which is defined as the RAPID-style AMOC from the model. This is an analog of how the RAPID calculation is made but not a direct replication as, in reality, moorings at a finite number of zonal locations as illustrated in Figure 4 are used to construct each profile. Our method does not take account of the potential for this reference level to change in a changing climate, which is a possibility [*Baehr et al.*, 2009]. However the fact that the RAPID-style AMOC reproduces well the full velocity derived AMOC indicates that this is not a major problem.

Essentially the same procedure is used to calculate a RAPID-style AMOC in HG2 with the following differences. Due to the lower resolution, the Florida Straits are not well represented in this model. The latitude of 29.5° was chosen for this investigation. The longitude chosen for the boundary of the WBW is 77.5°W and the reference level is at 4000 m in this model. The choice of the WBW limit is somewhat arbitrary. Choosing 77.5°W results in a good agreement in between the RAPID-style calculation and the full velocity calculation

Table 2. Models Used in This Study[a]

		Trend 2000–2100 RCP 4.5 (Sv decade^{-1})			Trend 2000–2100 RCP 8.5 (Sv decade^{-1})		
Model Name	Institute ID	Full AMOC	RAPID-Style	RS1000	Full AMOC	RAPID-Style	RS1000
ACCESS 1.0	CSIRO-BOM	−0.56	−0.66	0	−0.7	−0.85	−0.03
ACCESS 1.3	CSIRO-BOM	−0.36	−0.56	0.07	−0.62	−0.85	0
CSIRO-Mk3	CSIRO-QCCCE	−0.4	−0.48	0.16	−0.67	−0.75	−0.05
CanESM2	CCCMA	−0.19	−0.19	0.15	−0.33	−0.32	0.11
MPI-LR	MPI-M	−0.34	−0.32	−0.13	−0.72	−0.56	−0.36
MPI-MR	MPI-M	−0.76	−0.7	−0.18	−0.76	−0.7	−0.18
HadGEM2-ES	MOHC				−0.81	−0.51	−0.14
HadGEM3-GC2	MOHC	−0.75	−0.81	−0.65			

[a]Trends over the period 2000–2100 are shown.

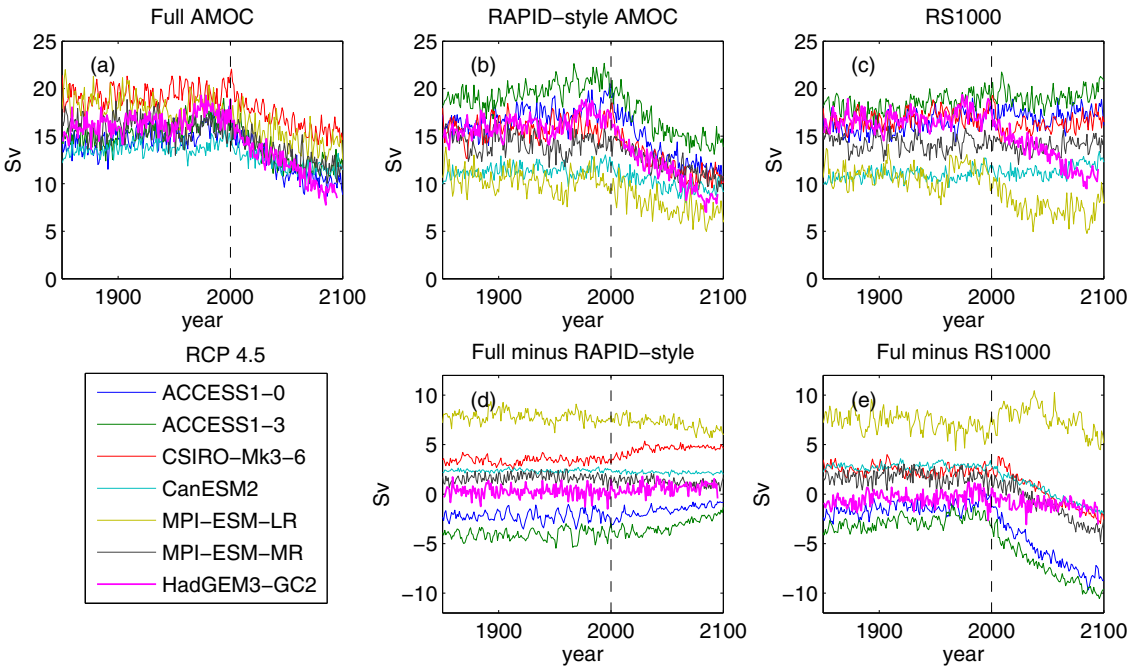

Figure 7. AMOC strength based on (a) full model velocities, (b) a RAPID-style calculation of the AMOC in the model, and (c) a RAPID-style calculation with values deeper than 1000 m held constant for a range of CMIP5 models and HadGEM3 under RCP4.5 forcing. Differences between calculations (a) and (b) are shown in Figure 7d. Differences between calculations (a) and (c) are shown in Figure 7e.

though the choice leads to a shallow ($z > -1000$) WBW contribution. Choosing the next grid point offshore, 76.75°W, results in less absolute agreement but better agreement in the variability.

The additional CMIP5 models are analyzed in less detail but with the intention to show that HG2 is representative of a range of CMIP5 models. There are a number of differences in the RAPID-style calculation applied to these models. The mid-Atlantic ridge is neglected, which has only a minor contribution. Ekman transport was also not explicitly calculated for these additional models. Instead ageostrophic velocities were estimated by taking the full velocities in the top 100 m and subtracting the geostrophic velocities. These ageostrophic velocities are dominated by and a good approximation of Ekman transport. The method proved accurate when tested using the explicitly calculated Ekman transport in the Hadley Centre models. The deepest level was chosen as the level of no motion. For each, the meridional grid index closest to 26.5°N was chosen to analyze. The limits for the WBW section were chosen as 77°W apart from the ACCESS models, which had a WBW limit at 80°W. The models have either a B-grid or a C-grid so temperature, salinity and velocity were all interpolated onto a common grid prior to analysis.

All of the models for both RCP 4.5 and RCP 8.5 show future decline in the strength of the AMOC from the full calculation (Figures 7a, 8a and Table 2) and were selected for this reason. The RAPID-style reconstruction succeeds well in reproducing the variability of the full AMOC in the historical run prior to 2000 and for the most part reproduces the projected changes (Figures 7b, 7d, 8b, 8d and Table 2). There are mean offsets due in part to the barotropic throughflow in the full AMOC calculation. There are a number of models that show differences in the projected AMOC: in the ACCESS runs and CSIRO-Mk3 runs, the RAPID style method slightly underestimates the AMOC (although the effect is transient in the case of the CSIRO model), whereas the RAPID-style calculation slightly overestimates in the case of the MPI-ESM-LR RCP 4.5 run and the HadGEM2-ES RCP 8.5 run. These differences are small in comparison to the changes that the RAPID-style calculation is replicating.

In contrast to the effective reproduction of AMOC variability by the full RAPID-style calculation, the RS1000 simulation fails to capture much of the future changes in the AMOC (Figures 7c, 7d and Table 2). With the exception of the HadGEM3 and MPI-ESM-LR runs, the future decline in the overturning is almost completely missed in the RS1000 calculations. This allows us to make the general statement that deep density gradient

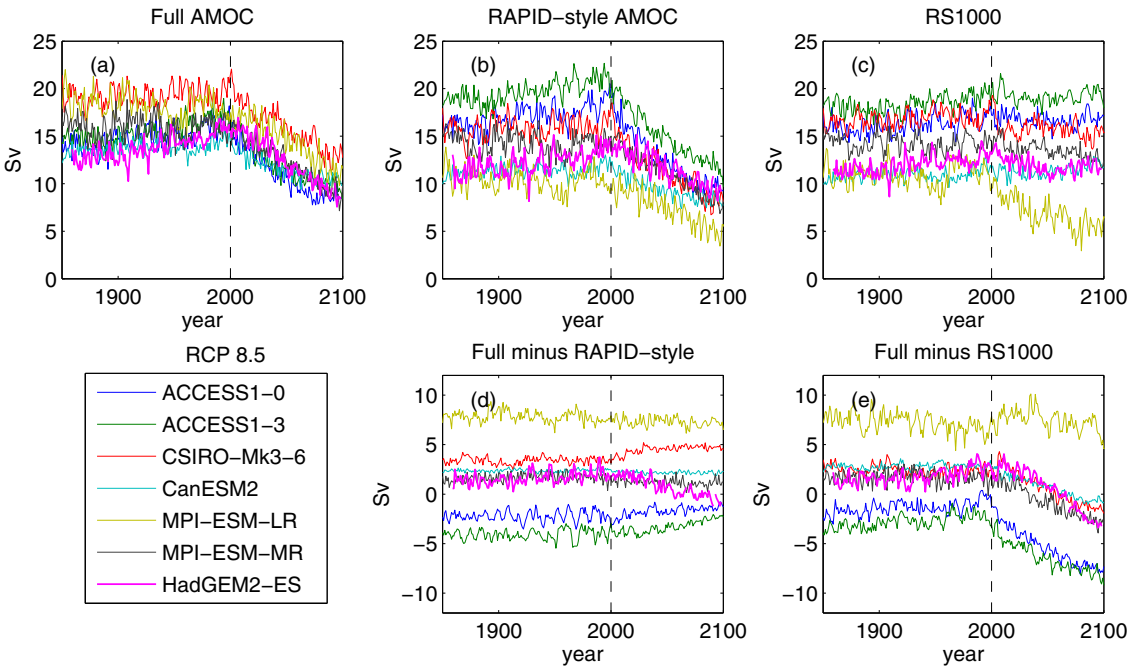

Figure 8. Same as Figure 7 but for RCP 8.5.

change is the predominant mechanism for overturning decline in the CMIP5 models analyzed. Deepwater formation is a problem in many coupled models with North Atlantic Deep Water (NADW) frequently being too shallow [*Legg et al.*, 2009]. Nonetheless, considering the transport deeper than 1000 m encapsulates the various representations of southward deep flow across the models and allows assessment of the partition of the flow between gyre and overturning.

We return to analyze the two HadGEM models in more detail. The strength of the AMOC in the HG2 model is 13.9 Sv prior to 2005 and the mean strength of the AMOC in the HG3 model is 16.4 Sv. Over the same time periods, the RAPID-style AMOC produces an AMOC strength that is 1.7 Sv weaker than the full AMOC in the HG2 model, whereas the HG3 RAPID-style calculation is only 0.2 Sv weaker than the full calculation. The RAPID-style calculation in both models reproduces the subdecadal variability well with correlations of 0.84 and 0.74 for HG2 and HG3, respectively.

As was previously seen, holding temperature and salinity constant below 1000 m in the HG2 model causes the decline in the AMOC after 2005 to be entirely missed (Figures 6a and 6c). The RS1000 calculation not only misses the future weakening but also the strengthening up to 2005 described by *Menary et al.* [2013]. In contrast to this, the RS1000 calculation in the HG3 model reproduces the AMOC variability well. The mean value for the strength of the AMOC is offset by 2.7 Sv relative to the RAPID-style calculation but all long-term trends are captured including the decline in the AMOC evident after the year 2000. For both models, the RS1000 calculation continues to reproduce the subdecadal variability well with correlations of 0.75 and 0.68 for HG2 and HG3, respectively, only a small drop from the full RAPID-style calculation.

The second configuration considered is a full deep mooring on the western boundary while measuring to a depth of 1500 m on the eastern boundary: the RSW configuration. In the HG2 model, the RSW calculation actually overestimates the AMOC decline after 2005 (Figures 9a and 9c). Much of the historical strengthening prior to 2005 is not captured by the RSW calculation. The RSW calculation results in a long-term drift toward an underestimation of the AMOC that accelerates post-2050. Consideration of the RSW calculation in the HG3 model results in increasing underestimates the AMOC throughout the run (Figures 9b and 9d). There is no change in the rate of change of the underestimation throughout the run and seems indicative of a long-term drift in the model.

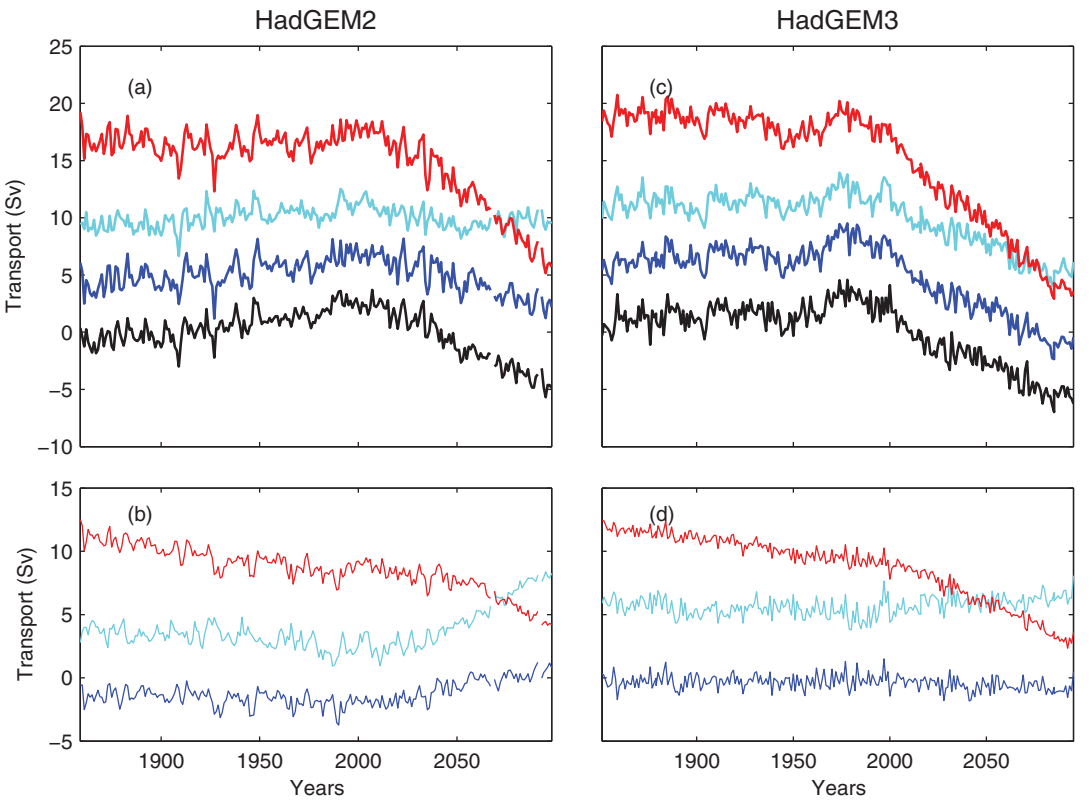

Figure 9. For the HG2 model run, (a) AMOC estimated from model velocities (black), RAPID style AMOC (blue), RS1000—RAPID style with values deeper than 1000 m held constant (cyan) and RSW—RAPID style with a full western boundary but only eastern boundary data to 1000 m (red). All values have had their mean subtracted, each subsequent calculation offset by 5 Sv. (b) Full AMOC minus RAPID style AMOC (blue), Full AMOC minus RS1000 (cyan) and Full AMOC minus RSW (red). Each subsequent calculation has been offset by 5 Sv. (c) and (d) Are the same cases as (a) and (b) but for the HG3 model run.

The origin of the changes in both these model runs can be understood by considering the changes in deep temperature, salinity, and density (Figure 10). Deeper than 1000 m, the circulation near 26°N is dominated by southward flow of North Atlantic Deep Water. This is a geostrophically balanced flow with higher densities on the west relative to the east at the same depth driving the large-scale southward flow. The mean density pattern is dominated by temperature, where isotherms sloping upwards toward the western boundary illustrate colder and hence denser water on the west than on the east (Figure 4).

Considering HG2 to begin with, there is a mean density difference between the eastern and western boundaries of 0.01 kg m^{-3} deeper than 1000 m, the decline in this density difference after 2005 reflects the changes occurring in the AMOC (Figure 10c). Holding these deep quantities constant results in none of the long-term changes in the full AMOC being reflected in the RS1000 calculation. In both the eastern and western basins, the deep density on the boundary decreases and the decline in the AMOC post-2005 is due to the density on western boundary declining more rapidly than on the east. This also explains the accelerated decline of the AMOC in the RSW calculation relative to the full AMOC. In the case of RSW, the decline in the western boundary density is not offset by the similar, albeit smaller, decline in eastern boundary density and the AMOC collapses rapidly. Note that if the calculation used deep eastern measurements and no deep western measurements, the AMOC would appear to strengthen.

Decomposing this density change into temperature and salinity shows that it is not only deep warming that drives AMOC changes in HG2. From 2005 to 2025, a decrease in the cross-basin temperature gradient deeper than 1000 m starts the AMOC decline (Figure 10a). However, from 2025 onwards, the decline in the salinity difference across the basin (Figure 10b) dominates the decrease in density and consequent AMOC collapse.

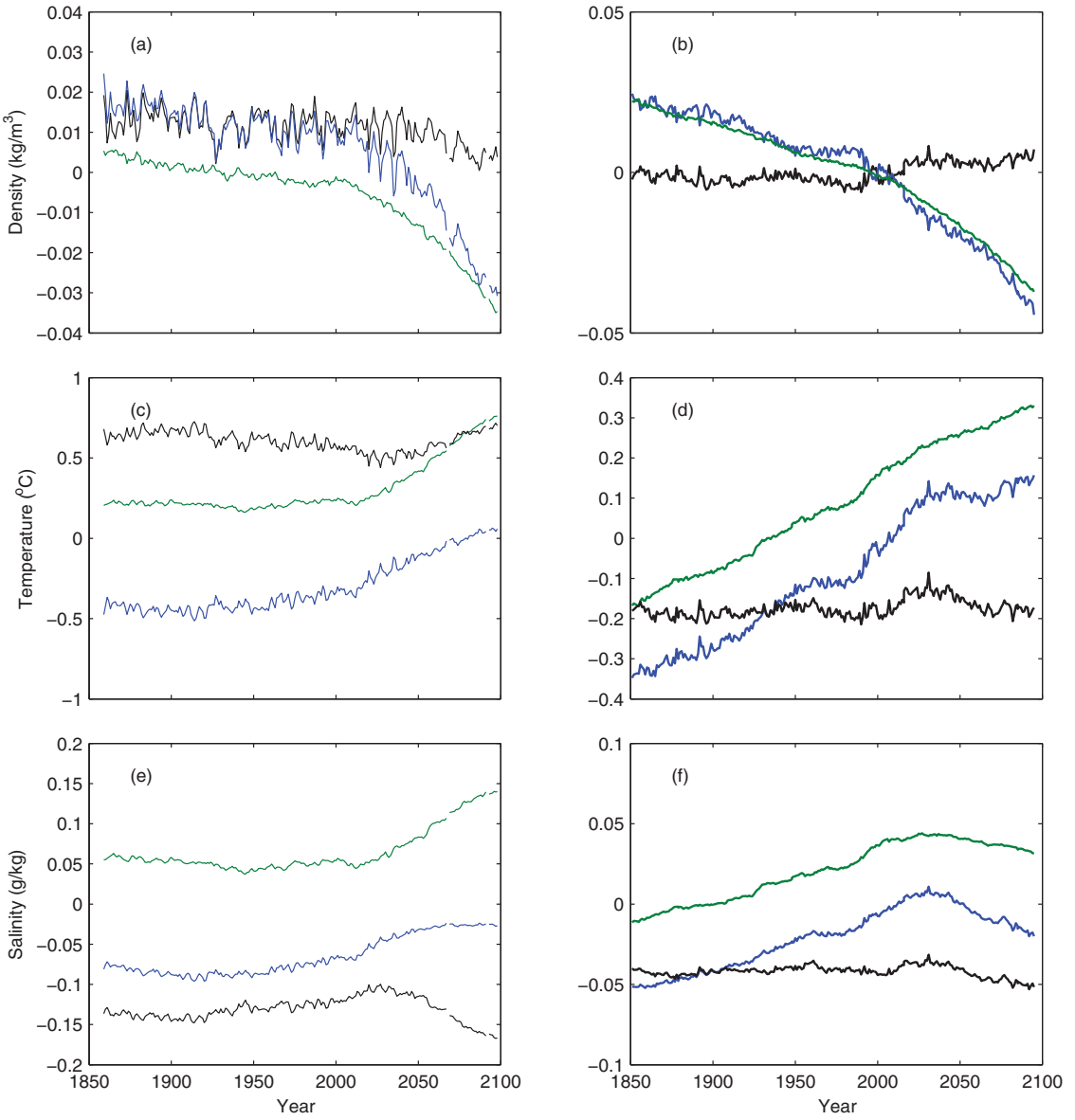

Figure 10. For the HG2 model run, (a) average density from the western (blue) and eastern (green) boundaries deeper than 1000 m and their difference (black). (c and e) Are the same but for potential temperature and salinity respectively. (b, d, and f) Are analogs of (a, c, and e) but for the HG3 model run. Note the changes in the extent of the *y* axis limits.

The AMOC changes in the HG3 model run are not dominated by the changes deeper than 1000 m as they are in HG2. Therefore, the deep density difference between eastern and western basins is relatively flat and close to zero at 0.002 kg m^{-3} throughout the run (Figure 10f). What is notable is that the density on both boundaries decreases at a similar rate. The RSW calculation estimates a continuously declining AMOC for HG3: the deep density on the west decreases and, with the deep east held constant, the cross-basin density contrast declines and so does the estimate of the AMOC.

Density changes deeper than 1000 m in HG3 in terms of temperature and salinity explains the density evolution. The deep temperature on both eastern and western boundaries rises throughout at a rate of 0.2° century^{-1}. The relatively constant rate of change in temperature is of concern and suggests that this may be a result of model drift or indicative of a model that is not fully spun up. The salinity on the other hand increases on both sides of the basin until approximately 2028 and decreases thereafter. Qualitatively similar changes occur on both sides of the basin with the western boundary salinity decreasing slightly more rapidly. However, these changes are not sufficient to significantly alter the AMOC in this model run.

5. Discussion

The vast majority of the subseasonal to decadal variability observed by the RAPID array in the AMOC since 2004 could be reproduced using a tall mooring on the west, such as WB2, that would not only provide a western boundary dynamic height profile but also an estimation of the WBW transport, and a single mooring in the east to 1500 m, such as EBH3. This is not altogether surprising given that density differences in the top 1000 m, particularly close to the eastern boundary, were noted to be the crucial signal for the seasonal cycle [*Pérez-Hernández et al*., 2015] and isopycnal displacements in the top 1000 m on the western boundary were crucial for the large interannual variability in 2009–2010 [*McCarthy et al*., 2012]. This provides a framework on which to base the delivery of real-time AMOC estimates from the array. We anticipate that these top 1000 m measurements would be sufficient to capture future reoccurrences of large interannual variability and future changes in the seasonal cycle, as these are primarily upper ocean responses to wind forcing. However, we argue that it is not an appropriate model for long-term observations capable of capturing a climate-time scale AMOC decline in the 21st century.

The development of a telemetry system that would deliver real-time data from the RAPID array is ongoing [*Rayner et al*., 2016]. The system, similar to systems in development elsewhere, is added to each mooring individually. Hence, for optimal deployment, the minimum number of moorings that can provide a useful estimate of the AMOC is important to know. Based on the observations thus far, telemetry of data from these two moorings would accurately estimate of interannual variability including the large downturn in 2009/2010. Near real-time AMOC data could thus aid the prediction of seasonal climate patterns [*Duchez et al*., 2015] and extreme sea level rise events [*Goddard et al*., 2015] and would provide a valuable estimate of the subclimate time scale AMOC variability.

The analysis of the 10 years of observations highlights two elements of the observing system that appear not to be critical in estimating AMOC variability on subclimate time scales. The use of regressed values of the WBW transport onto WB2 proved successful in reproducing the variability of the transports close to the Bahamas shelf. However, we note that this transport contributes significantly to the overall variability of the AMOC estimate (Figure 3). Regressions can change and were the regression to change in the future, this key area of variability could be misrepresented. Hence, the WBW measurements form a key element of the variability of the AMOC at this latitude. On the other hand, little variability was seen to arise from the Mid-Atlantic Ridge moorings. There is a mean density gradient across the ridge but this does not contribute to the AMOC variability observed since 2004. Furthermore, RAPID-style calculations in the HadGEM models that included or excluded the density gradient across the Mid-Atlantic Ridge did not show different projected behavior. The mid-Atlantic ridge supports northward flowing Antarctic Bottom Water (AABW) along its eastern flank. Climate models have problems simulating AABW in a similar way to NADW and it may be that variability due to this water mass does not exist because the models are deficient. Nonetheless, we must state that, in contrast to the WBW measurements, we have not been able to show a large contribution to the AMOC signal measured by the mid-Atlantic ridge moorings in either the observations or the climate models considered.

Looking in detail at our ability to detect a climate time scale AMOC decline through the prism of climate models, changes observed by such minimal arrays can be deceiving. The two models considered in detail here, both versions of the HadGEM climate model, differ widely. The older HG2 model has an AMOC that declines exclusively in the deep ocean as the cross-basin density difference erode and excluding estimates from deeper than 1000 m results in not capturing any AMOC decline. This is behavior typical of the range of CMIP5 models considered here and is implicit in the detectability study of *Baehr et al*. [2007]. On the other hand, in the newer HG3 model, the basinwide deep flow below 1000 m is weak due to a negligible cross-basin density difference and does not contribute to the AMOC decline. That is not to say that the deep ocean in HG3 does not change: it warms continually. In this case, the RSW configuration of moorings could lead to a marked and misleading overestimation of AMOC decline. Thus in neither model scenario would our suggested minimal array (based on the observation analysis), the RSW configuration, be appropriate to observe the AMOC decline. Full-depth measurements are therefore needed on both eastern and western basins to capture future climate-time scale AMOC decline. While this can be accomplished with a single mooring on the western boundary, a number of moorings are needed on the eastern boundary to both capture the near coast variability, crucial for the seasonal cycle [*Chidichimo et al*., 2010], and the deep variability farther offshore.

Satellite estimates of SSH primarily measure first baroclinic mode variability. Though not strictly comparable with either the *Frajka-Williams* [2015] or the *Willis* [2010] reconstructions, the RS1000 configuration is the most similar, focusing on the variations in the thermocline where the first baroclinic mode is most active *Szuts et al*. [2012]. The RS1000 configuration captures all the variability seen since 2004 in observations and was able to capture the subdecadal variability in the climate models. This is not a surprise as relatively simple two-layer, wind-driven models are also capable of capturing this variability [*Zhao and Johns*, 2014]. However, long-term deep changes in the AMOC driven by the deep circulation in HG2 and the majority of the CMIP5 models analyzed here are not captured by the RS1000 configuration and would not be captured by satellite-based proxies either. On the other hand, the RS1000 configuration did capture the HG3 AMOC decline and a satellite estimate would be able to capture this decline. Two pertinent questions that arise are which models' deep circulation is more like the real world and which type of AMOC decline is more likely?

To address the first of these questions, we look at the deep density patterns. The deep density difference between eastern and western boundaries in HG2 has an average of 0.01 kg m^{-3} prior to 2005 in comparison to 0.002 kg m^{-3} in HG3 (again prior to 2005). In HG2, it is this deep circulation that collapses the AMOC. The deep density in the RAPID observations over the same depth range shows a contrast between east and west of 0.02 kg m^{-3}. The observed density gradient is larger than either model, indicating that the real southward deep geostrophic flow of North Atlantic Deep Water is stronger than in both of these climate models. And, in fact, the newer model, HG3, is farther from reality than the older HG2.

We note that there are a number of model deficiencies that emerge also. The continual drift of the deep temperatures in the HG3 model of 0.4°C through the historical period (1850–2000) is likely to be an artifact of either model drift or indicative of a model that is not fully spun up. The HG3 model is the most modern model considered here and, consequently, the highest resolution. The problem of spinning up models becomes greater with higher and higher resolution. Potentially, all the AMOC decline being contained in the deep of the CMIP5 models is not realistic either. Given the role of the AMOC in upper ocean circulation, it is unlikely that there would not be a change in the circulation shallower than 1000 m, which is an implication of the results presented here.

The second question is more speculative. We are not going to consider in detail the origins of the AMOC collapses within these models. We will simply consider broadly the origins of an AMOC collapse. What sets the North Atlantic apart from the North Pacific in terms of deep circulation is the presence of (predominantly) two deepwater sources: that of Labrador Sea Water and Denmark Straits overflow water. At 26.5°N, these occupy depth ranges around 1100–3000 and 3000–5000 m. In different ways, these water masses contribute to the density gradient deeper than 1000 m and, were they to cease to form, the overturning would decline. Essentially, the North Atlantic would be more like the North Pacific, with no deep overturning circulation. The AMOC is a complex set of processes including not only deepwater formation but mixing, upwelling and water mass transformation driven by a combination of wind, buoyancy, and tidal forcing. In efforts to understand this complexity, it is important to remember that, if deepwater formation ceases, the overturning halts. This is the fundamental idea behind paleoceanography concepts of AMOC decline [e.g., *Broeker*, 1991] and some dramatic future projections of AMOC decline [e.g., *Hansen et al*., 2016]. If this is how the overturning declines in the future, we should be ready to observe this.

The deep ocean is one of the most poorly sampled elements of the climate system. This may change in the future with the advent of the deep Argo program [*Johnson et al*., 2015] and deep gliders [*Osse and Eriksen*, 2007] but currently deep ocean moorings are some of the few continuous observations at depth. There is a range of behaviors in deep circulation of the climate models considered here and no definitive way of knowing which—or even whether—one is right. Nonetheless, inadequately sampling the deep ocean in either model when estimating the AMOC can lead to very misleading results.

The AMOC is a fundamental metric of the climate system. How or whether it changes in response to anthropogenic forcing will be crucial to our understanding the dynamics and impacts of a changing climate. We are just over a decade into measuring the AMOC accurately with the RAPID array. AMOC variability on time scales from subseasonal [*Moat et al*., 2016] through seasonal [*Chidichimo et al*., 2010] to decadal [*Smeed et al*., 2014] have been discussed but no conclusions on AMOC decline due to anthropogenic climate change can yet be drawn. We draw an analogy with *Keeling* [1960], who discussed 2 years of CO_2 measurements at Mauna Loa, focusing on the seasonal cycle, which was the interesting feature of the

measurements when that time series was of that length. Over time, the Keeling curve that has documented the steady rise in atmospheric CO_2 in response to the burning of fossil fuels. Likewise, with the RAPID array, we expect the greatest impact of the measurements to be revealed over much longer time scales. In this paper we have emphasized the importance of deep, basinwide measurements in estimating the long-term evolution of the AMOC. It is crucial that, in an effort to be efficient, we do not remove elements from the observing system that are crucial to revealing future climatic changes.

Appendix A: Derivation of the Green's Function

The stream function for basinwide, geostrophic transports at a given latitude can be expressed as:

$$\Psi(z)=\frac{1}{\rho_0 f}\int_{z_R}^{z} dz' P(z'), \tag{A1}$$

where

$$P(z)=P_E(z)-P_W(z)$$

is the cross-basin pressure difference, ρ_0 is a reference density and f is the Coriolis parameter. The pressure can be expressed using the hydrostatic equation, which can be written in a slightly modified form using a simple Green's function:

$$P(z)=-g\int_{z_R}^{z} dz' \rho(z')=-g\int_{z_R}^{0} dz' \rho(z') G_P(z,z'), \tag{A2}$$

where

$$G_P(z,z')=\begin{cases} 1 & z>z' \\ 0 & z<z' \end{cases}. \tag{A3}$$

In this instance z_R is a reference level. This does not have to be at the ocean floor but for simplicity it will be set to this seafloor in this instance. The sea-surface is at $z=0$, with increasing negative values of z with depth.

The RAPID calculation enforces zero net flow across the basin. This is incorporated in a modified pressure term

$$P^*(z)=P(z)-\bar{P}w(z), \tag{A4}$$

where

$$\bar{P}=\frac{1}{A}\int_{z_R}^{0} dz' P(z') \tag{A5}$$

and

$$\int_{z_R}^{0} dz' w(z')=A, \tag{A6}$$

where A is the full area of the section and $w(z)$ is the width of the basin with depth. Hence, the modified pressure satisfies

$$\int_{z_R}^{0} P^*(z)dz=0. \tag{A7}$$

Combining equations (A2), (A4), and (A5) allows us to express

$$P^*(z)=-g\int_{z_R}^{0} dz' \rho(z') G_P(z,z')+g\frac{w(z)}{A}\int_{z_R}^{0} dz \int_{z_R}^{0} dz' \rho(z') G_P(z,z'). \tag{A8}$$

Switching the integral and noting that

$$\int_{z_R}^{0} dz G_P(z,z') = z', \tag{A9}$$

allows us to express

$$P^*(z) = -g\int_{z_R}^{0} dz'\,\rho(z')G_{P^*}(z,z'), \tag{A10}$$

where

$$G_{P^*}(z,z') = \begin{cases} 1-\dfrac{w(z)z'}{A} & z > z' \\ \dfrac{-w(z)z'}{A} & z < z' \end{cases}. \tag{A11}$$

Using the modified pressure and associated Green's function, we now express the stream function in equation (A1) as:

$$\Psi(z) = \frac{1}{\rho_0 f}\int_{z_R}^{z} dz' P^*(z') = -\frac{g}{\rho_0 f}\int_{z_R}^{0} dz''\rho(z'')\int_{z_R}^{z} G_{P^*}(z',z'')dz'. \tag{A12}$$

The integral of the modified pressure Green's function is then

$$G_\Psi(z,z') = \begin{cases} z - z' + \dfrac{A(z)}{A}z' & z > z' \\ \dfrac{A(z)}{A}z' & z < z' \end{cases}, \tag{A13}$$

where

$$A(z) = \int_{z_R}^{z} w(z')dz'$$

is the area from the seafloor to depth z. The fraction $A(z)/z$ is the fraction of the basin cross-section deeper than z, which has a value of 1 at the sea-surface and zero at the seafloor. This provides a framework to investigate how variations in density at a given level z' affect the overturning stream function at level z:

$$\Delta\Psi(z) = \frac{g}{\rho_0 f}\int_{z_R}^{0} dz' G_\Psi(z,z')\Delta\rho(z'). \tag{A14}$$

The AMOC is defined at the depth of the maximum of the overturning stream function. The change in this depth is given by

$$\Delta z_m \left.\frac{\partial P^*}{\partial z}\right|_{z=z_M} + \Delta P^*|_{z=z_M} = O(\Delta^2) \simeq 0. \tag{A15}$$

And the change in the AMOC is

$$\Delta\mathrm{AMOC} = \Delta\Psi|_{z=z_M} + \Delta z_M \left.\frac{\partial\Psi}{\partial z}\right|_{z=z_M} + O(\Delta\Psi^2), \tag{A16}$$

where the second term is zero because of the AMOC being defined as the maximum of the overturning stream function so

$$\left.\frac{\partial\Psi}{\partial z}\right|_{z=z_M} = 0.$$

Acknowledgments
The 26°N array is a collaborative effort supported through the UK Natural Environment Research Council (NERC) RAPID-AMOC program, the US National Science Foundation (NSF) Meridional Overturning Circulation Heat-flux Array project, and the US National Oceanographic and Atmospheric Administration (NOAA) Western Boundary Time Series project. Data from the RAPID-WATCH and MOCHA projects are freely available from www.rapid.ac.uk/rapidmoc and www.rsmas.miami.edu/users/mocha. Florida Current transports estimates are available from www.aoml.noaa.gov/phod/floridacurrent. We acknowledge the World Climate Research Programme's Working Group on Coupled Modelling, which is responsible for CMIP, and we thank the climate modeling groups (listed in Table 2 of this paper) for producing and making available their model output. For CMIP the U.S. Department of Energy's Program for Climate Model Diagnosis and Intercomparison provides coordinating support and led development of software infrastructure in partnership with the Global Organization for Earth System Science Portals. We would like to thank two anonymous reviewers and Joel Hirschi for their input which greatly improved this manuscript.

References

Baehr, J., J. Hirschi, J.-O. Beismann, and J. Marotzke (2004), Monitoring the Meridional Overturning Circulation in the North Atlantic: A model-based array design study, *J. Mar. Res.*, *62*(3), 283–312.

Baehr, J., H. Haak, S. Alderson, S. A. Cunningham, J. H. Jungclaus, and J. Marotzke (2007), Timely detection of changes in the Meridional Overturning Circulation at 26°N in the Atlantic, *J. Clim.*, *20*(23), 5827–5841.

Baehr, J., A. Stroup, and J. Marotzke (2009), Testing concepts for continuous monitoring of the Meridional Overturning Circulation in the South Atlantic, *Ocean Modell.*, *29*(2), 147–153.
Broeker, W. S. (1991), The great ocean conveyor, *Oceanography*, *4*(2), 79–89.
Bryden, H. L., and S. Imawaki (2001), Ocean heat transport, in *Ocean Circulation and Climate, Int. Geophys. Ser.*, vol. 77, edited by G. Siedler, J. Church, and J. Gould, 455–474, Academic Press, San Diego, Calif.
Bryden, H. L., H. R. Longworth, and S. A. Cunningham (2005), Slowing of the Atlantic Meridional Overturning Circulation at 25°N, *Nature*, *438*, 655–657.
Buchan, J., J. J.-M. Hirschi, A. T. Blaker, and B. Sinha (2014), North Atlantic SST anomalies and the cold north European weather events of winter 2009/10 and December 2010, *Mon. Weather Rev.*, *142*(2), 922–932.
Chidichimo, M. P., T. Kanzow, S. A. Cunningham, W. E. Johns, and J. Marotzke (2010), The contribution of eastern-boundary density variations to the Atlantic Meridional Overturning Circulation at 26.5°N *Ocean Sci.*, *6*, 475–490.
Collins, W., et al. (2011), Development and evaluation of an earth-system model-HadGEM2, *Geosci. Model Dev.*, *4*(4), 1051–1075.
Cunningham, S. A., et al. (2007), Temporal variability of the Atlantic Meridional Overturning Circulation at 26.5°N *Science*, *317*(5840), 935–938.
Dansgaard, W., S. Johnsen, H. Clausen, D. Dahl-Jensen, N. Gundestrup, C. Hammer, and H. Oeschger (1984), North Atlantic climatic oscillations revealed by deep Greenland ice cores, *Climate Processes and Climate Sensitivity, Geophys. Monogr. Ser.*, vol. 29, edited by J. E. Hansen and T. Takahashi, pp. 288–298, AGU, Washington, D. C.
Drijfhout, S., G. J. V. Oldenborgh, and A. Cimatoribus (2012), Is a decline of AMOC causing the warming hole above the North Atlantic in observed and modeled warming patterns?, *J. Clim.*, *25*, 8373–8379.
Duchez, A., P. Courtois, E. Harris, S. Josey, T. Kanzow, R. Marsh, D. Smeed, and J.-M. Hirschi (2015), Potential for seasonal prediction of Atlantic sea surface temperatures using the RAPID array at 26°N, *Clim. Dyn.*, *46*(9), 3351–3370.
Dunstone, N. J. (2014), A perspective on sustained marine observations for climate modelling and prediction, *Philos. Trans. R. Soc. London A*, *372*(2025), 20130340.
Fischer, J., M. Visbeck, R. Zantopp, and N. Nunes (2010), Interannual to decadal variability of outflow from the Labrador sea, *Geophys. Res. Lett.*, *37*, L24610, doi:10.1029/2010GL045321.
Fischer, M., A. Biastoch, E. Behrens, and J. Baehr (2013), Simulations of a line W-based observing system for the Atlantic Meridional Overturning Circulation, *Ocean Dyn.*, *63*(8), 865–880.
Frajka-Williams, E. (2015), Estimating the Atlantic overturning at 26 N using satellite altimetry and cable measurements, *Geophys. Res. Lett.*, *42*, 3458–3464, doi:10.1002/2015GL063220.
Frajka-Williams, E., S. A. Cunningham, H. Bryden, and B. A. King (2011), Variability of Antarctic Bottom Water at 24.5 N in the Atlantic, *J. Geophys. Res.*, *116*, C11026, doi:10.1029/2011JC007168.
Goddard, P. B., J. Yin, S. M. Griffies, and S. Zhang (2015), An extreme event of sea-level rise along the northeast coast of North America in 2009–2010, *Nature Commun.*, *6*, 6346 EP.
Hansen, J., et al. (2016), Ice melt, sea level rise and superstorms: Evidence from paleoclimate data, climate modeling, and modern observations that 2°C global warming could be dangerous, *Atmos. Chem. Phys.*, *16*(6), 3761–3812.
Hirschi, J., and J. Marotzke (2007), Reconstructing the Meridional Overturning Circulation from boundary densities and the zonal wind stress, *J. Phys. Oceanogr.*, *37*(3), 743–763.
Hirschi, J., J. Baehr, J. Marotzke, J. Stark, S. Cunningham, and J.-O. Beismann (2003), A monitoring design for the Atlantic Meridional Overturning Circulation, *Geophys. Res. Lett.*, *30*(7), 1413, doi:10.1029/2002GL016776.
Jackson, L., R. Kahana, T. Graham, M. Ringer, T. Woollings, J. Mecking, and R. Wood (2015), Global and European climate impacts of a slowdown of the AMOC in a high resolution GCM, *Clim. Dyn.*, *45*(11–12), 3299–3316.
Johns, W. E., L. M. Beal, M. O. Baringer, J. R. Molina, S. A. Cunningham, T. Kanzow, and D. Rayner (2008), Variability of shallow and deep western boundary currents off the Bahamas during 2004–05: Results from the 26 N RAPID-MOC array, *J. Phys. Oceanogr.*, *38*(3), 605–623, doi:10.1175/2007JPO3791.1.
Johns, W. E., et al. (2011), Continuous, array-based estimates of Atlantic ocean heat transport at 26.5°N, *J. Clim.*, *24*(10), 2429–2449, doi:10.1175/2010JCLI3997.1.
Johnson, G. C., J. M. Lyman, and S. G. Purkey (2015), Informing deep Argo array design using Argo and full-depth hydrographic section data, *J. Atmos. Oceanic Technol.*, *32*(11), 2187–2198.
Jones, C., et al. (2011), The HadGEM2-ES implementation of CMIP5 centennial simulations, *Geosci. Model Dev.*, *4*(3), 543–570.
Kanzow, T., S. A. Cunningham, D. Rayner, J. J.-M. Hirschi, W. E. Johns, M. O. Baringer, H. L. Bryden, L. M. Beal, C. S. Meinen, and J. Marotzke (2007), Observed flow compensation associated with the MOC at 26.5°N in the Atlantic, *Science*, *317*(5840), 938–941, doi:10.1126/science.1141293.
Kanzow, T., H. Johnson, D. Marshall, S. Cunningham, J.-M. Hirsch, A. Mujahid, H. Bryden, and W. Johns (2009), Basin wide integrated volume transports in an eddy-filled ocean, *J. Phys. Oceanogr.*, *39*, 3091–3110.
Keeling, C. D. (1960), The concentration and isotopic abundances of carbon dioxide in the atmosphere, *Tellus*, *12*(2), 200–203.
Landerer, F. W., D. N. Wiese, K. Bentel, C. Boening, and M. M. Watkins (2015), North Atlantic Meridional Overturning Circulation variations from GRACE ocean bottom pressure anomalies, *Geophys. Res. Lett.*, *42*, 8114–8121, doi:10.1002/2015GL065730.
Legg, S., et al. (2009), Improving oceanic overflow representation in climate models: The gravity current entrainment climate process team, *Bull. Am. Meteorol. Soc.*, *90*(5), 657–670.
Lozier, M. S., et al. (2016), Overturning in the subpolar North Atlantic program: A new international ocean observing system, *Bull. Am. Meteorol. Soc.*, doi:109/OCEANS.2007.4449125, in press.
Lynch-Stieglitz, J. (2001), Using ocean margin density to constrain ocean circulation and surface wind strength in the past, *Geochem. Geophys. Geosyst.*, *2*(12), 1069, doi:10.1029/2001GC000208.
Madec, G. (2008), *NEMO Ocean Engine*, Inst. Pierre-Simon Laplace (IPSL), France.
Maidens, A., A. Arribas, A. A. Scaife, C. MacLachlan, D. Peterson, and J. Knight (2013), The influence of surface forcings on prediction of the North Atlantic Oscillation regime of winter 2010/11, *Mon. Weather Rev.*, *141*(11), 3801–3813.
McCarthy, G., E. Frajka-Williams, W. E. Johns, M. O. Baringer, C. Meinen, H. Bryden, D. Rayner, A. Duchez, and S. A. Cunningham (2012), Observed interannual variability of the Atlantic Meridional Overturning Circulation at 26.5°N, *Geophys. Res. Lett.*, *39*, L19609, doi:10.1029/2012GL052933.
McCarthy, G., E. Gleeson, and S. Walsh (2015a), The influence of ocean variations on the climate of Ireland, *Weather*, *70*(8), 242–245.
McCarthy, G., D. Smeed, W. Johns, E. Frajka-Williams, B. Moat, D. Rayner, M. Baringer, C. Meinen, J. Collins, and H. Bryden (2015b), Measuring the Atlantic Meridional Overturning Circulation at 26°N, *Prog. Oceanogr.*, *31*, 91–111, doi:10.1016/j.pocean.2014.10.006.

McDonagh, E. L., B. A. King, H. L. Bryden, P. Courtois, Z. Szuts, M. Baringer, S. A. Cunningham, C. Atkinson, and G. McCarthy (2015), Continuous estimate of Atlantic oceanic freshwater flux at 26.5°N, *J. Clim.*, *28*(22), 8888–8906.

Megann, A., D. Storkey, Y. Aksenov, S. Alderson, D. Calvert, T. Graham, P. Hyder, J. Siddorn, and B. Sinha (2013), GO5.0: The joint NERC-Met Office NEMO global ocean model for use in coupled and forced applications, *Geosci. Model Dev. Discuss.*, *6*, 5747–5799.

Meinen, C. S., M. O. Baringer, and R. F. Garcia (2010), Florida current transport variability: An analysis of annual and longer-period signals, *Deep Sea Res., Part I*, *57*(7), 835–846.

Meinen, C. S., S. Speich, R. C. Perez, S. Dong, A. R. Piola, S. L. Garzoli, M. O. Baringer, S. Gladyshev, and E. J. Campos (2013), Temporal variability of the Meridional Overturning Circulation at 34.5S: Results from two pilot boundary arrays in the South Atlantic, *J. Geophys. Res. Oceans*, *118*, 6461–6478, doi:10.1002/2013JC009228.

Menary, M. B., C. D. Roberts, M. D. Palmer, P. R. Halloran, L. Jackson, R. A. Wood, W. A. Müller, D. Matei, and S.-K. Lee (2013), Mechanisms of aerosol-forced AMOC variability in a state of the art climate model, *J. Geophys. Res. Oceans*, *118*, 2087–2096, doi:10.1002/jgrc.20178.

Moat, B., et al. (2016), Major variations in subtropical North Atlantic heat transport at short (5 day) timescales and their causes, *J. Geophys. Res. Oceans*, *121*, 3237–3249, doi:10.1002/2016JC011660.

Osse, T. J., and C. C. Eriksen (2007), The deepglider: A full ocean depth glider for oceanographic research, in *OCEANS 2007*, pp. 1–12, IEEE, Washington, D. C.

Pérez-Hernández, M., G. McCarthy, P. Vélez-Belchí, D. Smeed, E. Fraile-Nuez, and A. Hernández-Guerra (2015), The Canary Basin contribution to the seasonal cycle of the Atlantic Meridional Overturning Circulation at 26°N, *J. Geophys. Res. Oceans*, *120*, 7237–7252, doi:10.1002/2015JC010969.

Rayner, D., S. Mack, P. Foden, M. Charcos-Llorens, and J. Campbell (2016), Development of the RAPID MK III telemetry system—A report on the NOC tank-testing and shallow and deep-water field trials, 54 pp., Natl. Oceanogr. Cent., Southampton, U. K.

Roberts, C. D., F. K. Garry, and L. C. Jackson (2013), A multimodel study of sea surface temperature and subsurface density fingerprints of the Atlantic Meridional Overturning Circulation, *J. Clim.*, *26*(22), 9155–9174.

Sato, M., J. E. Hansen, M. P. McCormick, and J. B. Pollack (1993), Stratospheric aerosol optical depths, 1850–1990, *J. Geophys. Res.*, *98*(D12), 22,987–22,994.

Send, U., M. Lankhorst, and T. Kanzow (2011), Observation of decadal change in the Atlantic Meridional Overturning Circulation using 10 years of continuous transport data, *Geophys. Res. Lett.*, *38*, L24606, doi:10.1029/2011GL049801.

Smeed, D., G. McCarthy, D. Rayner, B. Moat, W. Johns, M. Baringer, and C. Meinen (2015), *Atlantic Meridional Overturning Circulation Observed by the RAPID-MOCHA-WBTS (RAPID-Meridional Overturning Circulation and Heatflux Array-Western Boundary Time Series) Array at 26°N From 2004 to 2014*, Br. Oceanogr. Data Cent., Nat. Environ. Res. Counc., U. K.

Smeed, D. A., et al. (2014), Observed decline of the Atlantic Meridional Overturning Circulation 2004 to 2012, *Ocean Sci.*, *10*, 39–38.

Stocker, T. F., D. Qin, G.-K. Plattner, M. Tignor, S. K. Allen, J. Boschung, A. Nauels, V. B. Y. Xia, and P. M. M. (Eds.) (2013), *Climate Change 2013: The Physical Science Basis. Contribution of Working Group I to the Fifth Assessment Report of the Intergovernmental Panel on Climate Change*, Cambridge Univ. Press, Cambridge, U. K.

Szuts, Z., J. Blundell, M. Chidichimo, and J. Marotzke (2012), A vertical-mode decomposition to investigate low-frequency internal motion across the Atlantic at 26°N, *Ocean Sci.*, *8*, 345–367.

Taws, S. L., R. Marsh, N. C. Wells, and J. J.-M. Hirschi (2011), Re-emerging ocean temperature anomalies in late 2010 associated with a repeat negative NAO, *Geophys. Res. Lett.*, *38*, L20601, doi:10.1029/2011GL048978.

Williams, K., et al. (2015), The Met Office global coupled model 2.0 (GC2) configuration, *Geosci. Model Dev.*, *8*(5), 1509–1524.

Willis, J. K. (2010), Can in situ floats and satellite altimeters detect long-term changes in Atlantic ocean overturning?, *Geophys. Res. Lett.*, *37*, L06602, doi:10.1029/2010GL042372.

Zhang, R. (2008), Coherent surface-subsurface fingerprint of the Atlantic Meridional Overturning Circulation, *Geophys. Res. Lett.*, *35*, L20705, doi:10.1029/2008GL035463.

Zhao, J., and W. Johns (2014), Wind-forced interannual variability of the Atlantic Meridional Overturning Circulation at 26.5°N, *J. Geophys. Res. Oceans*, *119*, 2403–2419, doi:10.1002/2013JC009407.